General Geometry Calibration Using Arbitrary Free-form Surface in a Vision-based Robot System

He Xie, Wenlong Li and Hui Liu

***Abstract*—Geometry calibration is a critical problem in vision-based robot systems. The calibration objects of existing methods are limited to regular shapes. In this paper, a general calibration method using an arbitrary free-form surface is proposed to simultaneously calibrate the geometry parameters. By incorporating a shape matching algorithm, each measured point on the surface can be regarded as a feature point to compare with the design model for a closed-form initial solution and an iterative fine solution. In the objective function of fine solution, the residual is described by the point-to-tangent distance, and the solution is proved to be Gaussian-Newton method with second-order convergence. The geometry and matching errors are iteratively compensated to improve the calibration accuracy. The characteristics of the method are large number of feature points, no need for specific features, no limitations on the size of the free-form surface and convenient robot pose control. Finally, simulations and experiments verify the availability of the proposed method in the presence of measuring noise, robot repeated positioning error and a small number of robot poses.**

***Index Terms*—Vision-based robot, free-form surface, geometry calibration, hand-eye pose.**

NOMENCLATURE

Symbol	Definition
$\boldsymbol{Q}$	Robot kinematic parameters
$\{S, E, B, W\}$	Sensor frame, end-effector frame, base frame and world(design model) frame
${}^{N}_{M}\boldsymbol{T}$	4×4 pose matrix of frame $\{M\}$ with respect to reference frame $\{N\}$
${}^{W}_{B}\boldsymbol{T}$, ${}^{B}_{E}\boldsymbol{T}$, ${}^{E}_{S}\boldsymbol{T}$	Matching pose, robot pose and hand-eye pose
${}^{N}_{M}\boldsymbol{T}^{*}$	Designed value of ${}^{N}_{M}\boldsymbol{T}$
${}^{N}_{M}\boldsymbol{T}(\boldsymbol{\chi})$	${}^{N}_{M}\boldsymbol{T}$ is a function of parameter $\boldsymbol{\chi}$
${}^{N}_{M}\boldsymbol{R}$	3×3 rotation matrix in ${}^{N}_{M}\boldsymbol{T}$
${}^{N}\boldsymbol{E}_{M}$	3×1 Euler rotation vector of ${}^{N}_{M}\boldsymbol{R}$
${}^{N}\boldsymbol{t}_{M}$	3×1 translation vector in ${}^{N}_{M}\boldsymbol{T}$
$\Delta\boldsymbol{\chi}$	Error of parameter $\boldsymbol{\chi}$($\boldsymbol{\chi}$=$\boldsymbol{p}$, $\boldsymbol{T}$, $\boldsymbol{Q}$)
${}^{N}\boldsymbol{D}$	6×1 pose error vector of frame $\{N\}$ with respect to reference frame $\{N\}$
${}^{B}\boldsymbol{D}$, ${}^{E}\boldsymbol{D}$, ${}^{S}\boldsymbol{D}$	Matching, robot and hand-eye pose error vector
$\boldsymbol{\xi}$	Combined error vector of ${}^{B}\boldsymbol{D}$, $\Delta\boldsymbol{Q}$ and ${}^{S}\boldsymbol{D}$
${}^{N}\boldsymbol{d}$	3×1 translation error vector in ${}^{N}\boldsymbol{D}$
${}^{N}\boldsymbol{\delta}$	3×1 rotation error vector in ${}^{N}\boldsymbol{D}$
${}^{N}\boldsymbol{p}_i$	Measured position of point $\boldsymbol{p}_i$ in $\{N\}$
${}^{W}\boldsymbol{q}_i$	Designed position of point ${}^{W}\boldsymbol{p}_i$ in $\{W\}$
${}^{W}\hat{\boldsymbol{p}}_i$	Estimated position (${}^{W}\boldsymbol{p}_i$+Δ ${}^{W}\boldsymbol{p}_i$)
${}^{N}_{M}\hat{\boldsymbol{T}}$	Estimated pose (${}^{N}_{M}\boldsymbol{T}+\Delta{}^{N}_{M}\boldsymbol{T}$)
${}^{N}P$, ${}^{N}Q$	Measured point set and design model in $\{N\}$
$\varepsilon(\chi)$	Calibration error $\|\|\chi-\chi^{*}\|\|$of pose vector χ
e_i	Residual (distance error) from $\boldsymbol{p}_i$ to design model

I. INTRODUCTION

AS computer vision and robot technique has developed, vision-based robot systems are increasingly used in many applications, such as grinding, milling [3], drilling [4], welding [5, 6], grasping [7], remote handling [8], inspection [9-11] and surgery [12-14]. A robot equipped with a vision sensor is able to operate the object flexibly without manual intervention. To guide accurate robot operation, the calibration accuracy of geometry parameters (hand-eye pose and kinematic parameters) often needs to be ensured. However, the calibration is affected by many factors, such as the calibration object, the measuring noise, and the coupling effect between the hand-eye pose and kinematic parameters.

According to the types of geometry parameters, geometry calibration includes three categories: robot kinematic calibration, hand-eye calibration and simultaneous calibration. The kinematic calibration is related to kinematic models, such as the Denavit–Hartenberg (D-H) model [15] and the product of exponentials (POE) model [16]. In the POE-based calibration method, there is no discontinuity in the kinematic parameters of parallel adjacent joints, but the relationship between the kinematic parameters and the exponential product needs to be built. The basic hand-eye calibration problem is usually concluded as the solution of the homogenous transformation equation $\boldsymbol{AX}=\boldsymbol{XB}$, where $\boldsymbol{A}$ is the relative pose of the robot end-effector between two different robot poses, $\boldsymbol{B}$ is the relative pose of the sensor between two different robot poses, and $\boldsymbol{X}$ is the unknown hand-eye pose including the orientation and position [17]. According to the expression for the solution, hand-eye calibration can be divided into a closed-form solution and an iterative solution [18, 19]. The closed-form solution is fast but sensitive to noise and data scale. The iterative solution is accurate but slow. In the individual hand-eye calibration method, kinematic errors may also cause error propagation in hand-eye calibration. However, simultaneous calibration of

This work is supported by the National Natural Science Foundation of China (No. 61733004, 52090054, 52075203), the China National Postdoctoral Program for Innovative Talents (No. BX2021098) and the Hubei Province Key Research and Development Plan (Grant No. 2020BAA025). (Corresponding author: Wenglong Li)

He Xie is with the National Engineering Laboratory for Robot Visual Perception and Control Technology, Hunan University, Changsha, China. (E-mails: xiehe@hust.edu.cn)

Wenglong Li is with the State Key Laboratory of Digital Manufacturing Equipment and Technology, Huazhong University of Science and Technology (HUST), Wuhan, China (E-mails: wlli@hust.edu.cn).

Hui Liu is with the School of Traffic and Transportation Engineering, Central South University, Changsha, China(E-mail: csuliuhui@csu.edu.cn)

both hand-eye pose and kinematic parameters can reduce the error propagation. The multiple sensor information fusion technique can also deal with uncertain noise and external error disturbance for accurate pose estimation. For example, Du *et al.* [20, 21] used Kalman filters and particle filters to control liner Gaussian and nonlinear disturbances for posture estimation, respectively. Experiments of a robot screwing in a bolt show the validity of the method.

In addition to the basic problem of geometry calibration, the application of calibration methods is also related to the calibration object. Geometry parameters are usually calibrated by measuring specific features (points, lines, etc.) on the calibration object to construct an objective function or space constraint equation. A standard sphere is usually used as a calibration object because the sphere center position can be easily calculated by fitting the spherical measured points from a surface scanner or fitting the circular measured points from a linear laser scanner. In the sphere-based method, the hand-eye position and orientation can be calibrated separately. First, the robot is translated along three coordinate axes to measure the sphere center for orientation calibration. Second, the position is calibrated when the robot is controlled to move with different orientations [10, 22], poses [23] or rotation along the coordinate axes [2]. When the sphere is used for simultaneous geometry calibration, it is usually necessary to build the equations denting the measured center position in a set of different robot poses [1, 9, 24]. The sphere can also be used to calibrate the kinematic parameters of both the robot and the additional movement module. Integrating an industrial robot with a turntable and a linear laser scanner, Li *et al.* [22] developed a laser scanning system with 7 degrees of freedom. A sphere is fixed on the turntable to calibrate both turntable pose and hand-eye pose. Yin *et al.* [9] developed a large-scale robot scanning system by fixing a linear rail on the end-effector and fixing the laser scanner on the rail. The robot kinematic parameters, rail orientation and hand-eye pose were calibrated using a sphere. The sphere-based method is simple, but the sphere size is limited by the scope of the vision sensor to ensure sphere fitting accuracy.

The geometry parameters can also be calibrated by planes [25-27], disks [28], pins [29, 30], crosshair objects [31] and crenellated objects [11]. In [32], the intersection point of the projected laser lines on a plane is regarded as a feature point to simultaneously calibrate the camera intrinsic parameters and the hand-eye pose. Robertsson *et al.* [25] used three planes for eye-to-hand calibration. The three planes were placed surrounding the robot to be approximately orthogonal to each other. The plane equation and the space transformation between the planes were iteratively calculated using two-step method. Sharifzadeh *et al.* [27] further proposed a single-plane method to reduce the complexity of the calibration process. Chen *et al.* [28] used a circular disk to calibrate the hand-eye pose of a linear laser scanner. The disk center is used as a feature point. The center position is calculated according to the disk radius and the width of the projected laser on the disk. Using a pin, Franke *et al.* [29] proposed a self-calibration method of a linear laser scanner. The laser line should pass through the pin tip by a search strategy. Lembono *et al.* [30] used a plane with two small holes and a pin mounted on the end-effector to calibrate the kinematic parameters of the robot and the extrinsic parameters of the laser projector. The robot is moved to ensure that the tip touches two holes on the plane. In the robotic inspection system with a laser sensor [31], the kinematic errors are estimated using crosshair objects. The crosshair center and the laser stripe centerline are extracted in the image captured by the camera of the sensor. The robot is controlled to ensure that the crosshair center passes through the centerline.

The above methods vary with the calibration object with specific shapes. This paper uses a free-form surface as the calibration object. A coarse-to-fine calibration method is proposed to simultaneously calibrate the hand-eye pose and kinematic parameters. A closed-form initial solution and an iterative fine solution are derived. Compared to previous work [1], the proposed method is enhanced by incorporating shape matching between the measured points and the design model, ensuring that each measured point on the surface can be used as a feature point. The point-to-tangent distance [33] is used to express the residual between the estimated and designed position, ensuring second-order convergence speed rather than linear speed in the sphere-based method [1]. Fine calibration includes four stages: 1) Error modeling. The mathematical relationship between the reconstructed error of each measured point and the geometry errors/matching errors is built using the speed adjoint transformation. 2) Data acquisition. The calibration process only requires that the robot end-effector moves randomly to collect a set of measured points and the corresponding robot poses. 3) Error identification. The geometry errors and matching errors are simultaneously identified by minimizing the squared sum of the reconstructed position error to avoid the correlation effect between the pose errors. 4) Error compensation. The identified errors are compensated for the next iteration. The characteristics of the proposed calibration method using free-form surface are as follows. 1) Compared with the sphere, free-form surface has large number of feature points (>10, 000) to construct the objective function, helping improve the calibration performance. 2) The fine calibration process is simple and convenient. There is no need for strict control of both orientation and position, allowing scanning data collected from random robot poses. 3) Arbitrary workpieces (such as propellers, blades, cranks and pipes) can be used as calibration object, avoiding the expense of machining specific shapes/feature. The size of the free-form surface is also not limited by the scope of the vision sensor, which is appropriate for large space calibration.

This paper is organized as follows. The kinematic model of the vision-based robot system is built in Section II. Coarse and fine calibration methods using a free-form surface are proposed in Sections III and IV, respectively. Simulations and experiments are performed in Sections V and VI, respectively. This paper is concluded in Section VII.

This article has been accepted for publication in a future issue of this journal, but has not been fully edited. Content may change prior to final publication. Citation information: DOI 10.1109/TIE.2021.3090716, IEEE Transactions on Industrial Electronics

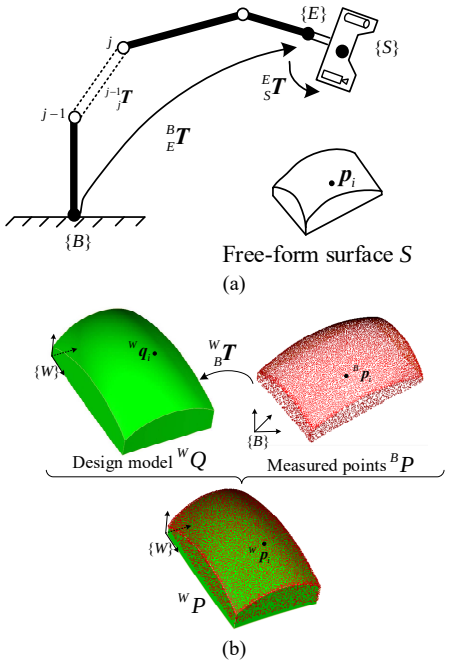

Fig. 1. Vision-based robot system. (a) Schematic of the system using an arbitrary free-form surface as calibration object. (b) Free-form surface matching. The design model is defined in world frame $\{W\}$. Measured point set ${}^{B}P$ is matched with the design model ${}^{W}Q$ to calculate the matching pose ${}^{W}_{B}\boldsymbol{T}$. The objective function is $\min\ f({}^{W}_{B}\boldsymbol{T}) = \sum \| {}^{W}_{B}\boldsymbol{T}\,{}^{B}\boldsymbol{p}_i - {}^{W}\boldsymbol{q}_i \|^2$.

II. Kinematic Model of a Vision-based Robot System

The vision-based robot system is shown in Fig. 1(a). A vision sensor with coordinate frame $\{S\}$ is fixed in the robot end-effector with frame $\{E\}$. The free-form surface is fixed in the robot base with frame $\{B\}$. The pose of the general frame $\{M\}$ with respect to reference frame $\{N\}$ is defined as the 4×4 homogeneous transformation matrix ${}^{N}_{M}\boldsymbol{T}$. The homogeneous coordinate of a measured point $\boldsymbol{p}$ in frame $\{S\}$ is defined as ${}^{S}\boldsymbol{p}=[{}^{S}p_x, {}^{S}p_y, {}^{S}p_z, 1]^{\mathrm{T}}$. Then the reconstructed point in frame $\{B\}$ can be written as

$$ {}^{B}\boldsymbol{p} = {}^{B}_{E}\boldsymbol{T}\,{}^{E}_{S}\boldsymbol{T}\,{}^{S}\boldsymbol{p} \tag{1} $$

where symbol ${}^{E}_{S}\boldsymbol{T}$ denotes the hand-eye pose of the sensor frame $\{S\}$ with respect to end-effector frame $\{E\}$ and symbol ${}^{B}_{E}\boldsymbol{T}$ denotes the robot pose of end-effector frame $\{E\}$ with respect to base frame $\{B\}$. For a robot with m joints, pose ${}^{B}_{E}\boldsymbol{T}$ can be expressed as ${}^{B}_{E}\boldsymbol{T}=\prod_{j=1}^{m} {}^{j-1}_{j}\boldsymbol{T}$, where ${}^{j-1}_{j}\boldsymbol{T}$ denotes the adjacent pose of the joint frame $\{j\}$. According to the D-H model, the adjacent pose can be written as ${}^{j-1}_{j}\boldsymbol{T}(a_{j-1},\alpha_{j-1},d_j,\theta_j)$. Then the kinematic vector becomes

$$ \boldsymbol{Q}_{4m\times1} = [a_0,\alpha_0,d_1,\theta_1,\cdots,a_{m-1},\alpha_{m-1},d_m,\theta_m]^{\mathrm{T}} = [q_1,q_2,\cdots,q_{4m}]^{\mathrm{T}} \tag{2} $$

Thus, the geometry parameters include the kinematic parameters $\boldsymbol{Q}$ and the hand-eye pose ${}^{E}_{S}\boldsymbol{T}$. In general, the robot base frame $\{B\}$ is defined as the world frame for calibration. However, the position ${}^{B}\boldsymbol{p}$ of the feature point before calibration is unknown due to random placement of the calibration object. In this case, the position error $\| {}^{B}\boldsymbol{p}_i - {}^{B}\boldsymbol{p}_{i+1} \|$ in different robot poses $({}^{B}_{E}\boldsymbol{T}_i, {}^{B}_{E}\boldsymbol{T}_{i+1})$ is usually minimized to calibrate the kinematic parameters $\boldsymbol{Q}$ and hand-eye pose ${}^{E}_{S}\boldsymbol{T}$ in (1). To conveniently find the feature point on the calibration object, the feature point is usually designed in the center of specific geometry object. Thus, the number of feature points is limited by the specific features. Since the geometry center usually does not have specific normal vector, the position error is mainly expressed as Euclidean distance, which shows only linear convergence in the iteration.

In this paper, the design model frame of the free-form surface is defined as the world frame $\{W\}$ in Fig. 1(b). The reconstructed point in frame $\{W\}$ is

$$ {}^{W}\boldsymbol{p} = {}^{W}_{B}\boldsymbol{T}\,{}^{B}\boldsymbol{p} = {}^{W}_{B}\boldsymbol{T}\,{}^{B}_{E}\boldsymbol{T}\,{}^{E}_{S}\boldsymbol{T}\,{}^{S}\boldsymbol{p} \tag{3} $$

where symbol ${}^{W}_{B}\boldsymbol{T}$ denotes the matching pose of base frame $\{B\}$. Pose ${}^{W}_{B}\boldsymbol{T}$ can be obtained by shape matching the measured point set ${}^{B}P = \{{}^{B}\boldsymbol{p}_1,\cdots,{}^{B}\boldsymbol{p}_i,\cdots{}^{B}\boldsymbol{p}_n\}$ with the design model ${}^{W}Q$ [33]. After matching, the measured point set ${}^{W}P$ in frame $\{W\}$ is obtained using (3). It is obvious that each position ${}^{W}\boldsymbol{p}_i$ in frame $\{W\}$ is unrelated to the position of the placed calibration object in base frame $\{B\}$. The closest point ${}^{W}\boldsymbol{q}_i$ of ${}^{W}\boldsymbol{p}_i$ in the design model can also be easily found by the nearest point search algorithm, such as the kdtree algorithm [32]. Thus, all measured points in ${}^{W}P$ can be used as feature points to construct the calibration equation $\| {}^{W}\boldsymbol{p}_i - {}^{W}\boldsymbol{q}_i \| = 0$.

III. Coarse Calibration Using Free-form Surface

To achieve accurate geometry calibration using a free-form surface, the proposed calibration method includes two steps: coarse and fine calibration. 1) Coarse calibration roughly calibrates hand-eye pose ${}^{E}_{S}\boldsymbol{T}$ and matching pose ${}^{B}_{W}\boldsymbol{T}$. 2) Using the coarse calibrated result as an initial value, fine calibration precisely identifies the hand-eye pose error $\Delta{}^{E}_{S}\boldsymbol{T}$, robot kinematic errors $\Delta\boldsymbol{Q}$ and matching pose error $\Delta{}^{B}_{W}\boldsymbol{T}$, corresponding to the final fine calibration result ${}^{E}_{S}\boldsymbol{T}+\Delta{}^{E}_{S}\boldsymbol{T}$, ${}^{B}_{W}\boldsymbol{T}+\Delta{}^{B}_{W}\boldsymbol{T}$ and ${}^{B}_{E}\boldsymbol{T}(\boldsymbol{Q}+\Delta\boldsymbol{Q})$, respectively.

When the robot pose is ${}^{B}_{E}\boldsymbol{T}_i$, the obtained measured point set in frame $\{S\}$ is defined as ${}^{S}P_i$, which is matched with the design model ${}^{W}Q$ to obtain the sensor pose ${}^{W}_{S}\boldsymbol{T}_i$ with respect to world frame $\{W\}$. According to (3), pose ${}^{W}_{S}\boldsymbol{T}_i$ can be written as

$$ {}^{W}_{S}\boldsymbol{T}_i = {}^{W}_{B}\boldsymbol{T}\,{}^{B}_{E}\boldsymbol{T}_i\,{}^{E}_{S}\boldsymbol{T} \tag{4} $$

The sensor is fixed on the robot end-effector, and the free-form surface is fixed on the base frame $\{B\}$. Thus, the hand-eye pose ${}^{E}_{S}\boldsymbol{T}$ and the matching pose ${}^{W}_{B}\boldsymbol{T}$ are unrelated to the robot pose ${}^{B}_{E}\boldsymbol{T}_i$. A general pose matrix is defined as

$$ {}^{N}_{M}\boldsymbol{T} = \begin{bmatrix} {}^{N}_{M}\boldsymbol{R} & {}^{N}\boldsymbol{t}_M \\ \boldsymbol{0}_{1\times3} & 1 \end{bmatrix} \tag{5} $$

where ${}^{N}_{M}\boldsymbol{R} \in SO(3)$ and ${}^{N}\boldsymbol{t}_{M} \in \Re^3$ are the rotation matrix and translation vector, respectively. According to (5), equation (4) can be written as

$$\begin{bmatrix} {}^{W}_{S}\boldsymbol{R}_i & {}^{W}\boldsymbol{t}_{Si} \\ \boldsymbol{0}_{3\times1} & 1 \end{bmatrix} = \begin{bmatrix} {}^{W}_{B}\boldsymbol{R} & {}^{W}\boldsymbol{t}_{B} \\ \boldsymbol{0} & 1 \end{bmatrix} \begin{bmatrix} {}^{B}_{E}\boldsymbol{R}_i & {}^{B}\boldsymbol{t}_{Ei} \\ \boldsymbol{0} & 1 \end{bmatrix} \begin{bmatrix} {}^{E}_{S}\boldsymbol{R} & {}^{E}\boldsymbol{t}_{S} \\ \boldsymbol{0} & 1 \end{bmatrix} \tag{6}$$

The nominal robot pose (${}^{B}_{E}\boldsymbol{R}_i$, ${}^{B}\boldsymbol{t}_{Ei}$) can be obtained from the robot controller. The pose (${}^{W}_{S}\boldsymbol{R}_i$, ${}^{W}\boldsymbol{t}_{Si}$) can be obtained by shape matching. Thus, there are four pose variables (${}^{W}_{B}\boldsymbol{R}$, ${}^{E}_{S}\boldsymbol{R}$, ${}^{W}\boldsymbol{t}_{B}$, ${}^{E}\boldsymbol{t}_{S}$) to be calibrated, which are introduced below. By expanding above equation, there is

$${}^{W}_{S}\boldsymbol{R}_i = {}^{W}_{B}\boldsymbol{R}\,{}^{B}_{E}\boldsymbol{R}_i\,{}^{E}_{S}\boldsymbol{R} \tag{7}$$

$${}^{W}\boldsymbol{t}_{Si} = {}^{W}_{B}\boldsymbol{R}\,{}^{B}_{E}\boldsymbol{R}_i\,{}^{E}\boldsymbol{t}_{S} + {}^{W}_{B}\boldsymbol{R}\,{}^{B}\boldsymbol{t}_{Ei} + {}^{W}\boldsymbol{t}_{B} \tag{8}$$

The robot orientation ${}^{B}_{E}\boldsymbol{R}_i$ remains invariable, and the robot position is translated from ${}^{B}\boldsymbol{t}_{Ei1}$ to ${}^{B}\boldsymbol{t}_{Ei2}$. According to (8), there is

$${}^{W}\boldsymbol{t}_{Si1} - {}^{W}\boldsymbol{t}_{Si2} = {}^{W}_{B}\boldsymbol{R}({}^{B}\boldsymbol{t}_{Ei1} - {}^{B}\boldsymbol{t}_{Ei2}) \tag{9}$$

When the robot is translated along multiple directions, the rotation matrix ${}^{W}_{B}\boldsymbol{R}$ can be solved. To satisfy the property (${}^{W}_{B}\boldsymbol{R} \in SO(3)$) of a standard rotation matrix, matrix ${}^{W}_{B}\boldsymbol{R}$ can be further optimized by the iterative method [23]. For an initial standard matrix of ${}^{W}_{B}\boldsymbol{R}$, it is assumed there is a differential rotation transformation between the initial and non-standard matrix. By multiple iterations of solving the differential rotation vector and compensating to the initial standard rotation matrix, the initial one would converge to a stable and optimal standard matrix. The solved standard matrix ${}^{W}_{B}\boldsymbol{R}$ is substituted into (7), and the hand-eye rotation matrix can be solved as ${}^{E}_{S}\boldsymbol{R} = {}^{B}_{E}\boldsymbol{R}_i^{-1}\,{}^{W}_{B}\boldsymbol{R}^{-1}\,{}^{W}_{S}\boldsymbol{R}_i$. To solve vectors (${}^{E}\boldsymbol{t}_{S}$, ${}^{W}\boldsymbol{t}_{B}$), equation (8) is rewritten as

$${}^{W}\boldsymbol{t}_{Si} = [{}^{W}_{B}\boldsymbol{R}\,{}^{B}_{E}\boldsymbol{R}_i, \boldsymbol{I}_{3\times3}] \begin{bmatrix} {}^{E}\boldsymbol{t}_{S} \\ {}^{W}\boldsymbol{t}_{B} \end{bmatrix} + {}^{W}_{B}\boldsymbol{R}\,{}^{B}\boldsymbol{t}_{Ei} \tag{10}$$

The robot orientation is changed to obtain multiple of the above equations to simultaneously solve vectors (${}^{E}\boldsymbol{t}_{S}$, ${}^{W}\boldsymbol{t}_{B}$). Since a large number of feature points ${}^{S}P_i$ are used for matching, the free-form surface in this coarse calibration process helps improve the calibration accuracy, compared to the sphere-based method with one feature point. However, the robot pose error $\Delta\,{}^{E}_{S}\boldsymbol{T}$ caused by the kinematic errors $\Delta\boldsymbol{Q}$ is still not considered. According to (6) and (10), the robot pose error $\Delta\,{}^{B}_{E}\boldsymbol{T}$ would cause the matching pose error $\Delta\,{}^{W}_{B}\boldsymbol{T}$ and hand-eye pose error $\Delta\,{}^{E}_{S}\boldsymbol{T}$. Thus, there is a correlation between the above three pose errors. To improve the calibration accuracy, three pose errors ($\Delta\,{}^{W}_{B}\boldsymbol{T}$, $\Delta\,{}^{B}_{E}\boldsymbol{T}$, $\Delta\,{}^{E}_{S}\boldsymbol{T}$) are simultaneously identified and compensated in fine calibration process.

IV. Fine Calibration Using Free-form Surface

The principle of the fine calibration process is as follows. 1) Geometry error modeling. The mathematical relationship between the position error $\Delta\,{}^{W}\boldsymbol{p}$ and the geometry error vectors (hand-eye pose error vector ${}^{S}\boldsymbol{D}$, kinematic error vector $\Delta\boldsymbol{Q}$, matching pose error vector ${}^{B}\boldsymbol{D}$) is constructed. 2) Geometry error identification. The squared sum of the reconstructed position error is minimized to identify the geometry errors. 3) Geometry error compensation. The identified geometry errors are used to calculate the fine geometry parameters (${}^{E}_{S}\boldsymbol{T} + \Delta\,{}^{E}_{S}\boldsymbol{T}({}^{S}\boldsymbol{D})$, ${}^{B}_{E}\boldsymbol{T}(\boldsymbol{Q} + \Delta\boldsymbol{Q})$ and ${}^{W}_{B}\boldsymbol{T} + \Delta\,{}^{W}_{B}\boldsymbol{T}({}^{B}\boldsymbol{D})$).

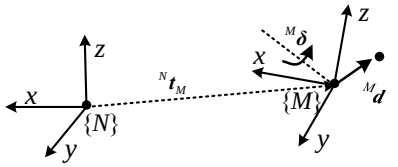

Fig. 2. Schematic of pose error vector

A. Geometry error modeling

In world frame $\{W\}$, the error equation of (3) can be written as

$${}^{W}\boldsymbol{p} + \Delta\,{}^{W}\boldsymbol{p} = \underbrace{({}^{W}_{B}\boldsymbol{T} + \Delta\,{}^{W}_{B}\boldsymbol{T})}_{\text{Part 3}} \underbrace{({}^{B}_{E}\boldsymbol{T} + \Delta\,{}^{B}_{E}\boldsymbol{T})}_{\text{Part 2}} \underbrace{({}^{E}_{S}\boldsymbol{T} + \Delta\,{}^{E}_{S}\boldsymbol{T})}_{\text{Part 1}} {}^{S}\boldsymbol{p} \tag{11}$$

where $\Delta\,{}^{W}\boldsymbol{p}$ is the reconstructed position error caused by three pose errors. By ignoring the second and higher-order error items, equation (11) becomes

$$\begin{aligned} \Delta\,{}^{W}\boldsymbol{p} &= \underbrace{\Delta\,{}^{W}_{B}\boldsymbol{T}\,{}^{B}_{S}\boldsymbol{T}\,{}^{S}\boldsymbol{p}}_{\text{Part3}} + \underbrace{{}^{W}_{B}\boldsymbol{T}\Delta\,{}^{B}_{E}\boldsymbol{T}\,{}^{E}_{S}\boldsymbol{T}\,{}^{S}\boldsymbol{p}}_{\text{Part2}} + \underbrace{{}^{W}_{E}\boldsymbol{T}\Delta\,{}^{E}_{S}\boldsymbol{T}\,{}^{S}\boldsymbol{p}}_{\text{Part1}} \\ &= \Delta\,{}^{W}\boldsymbol{p}_3 + \Delta\,{}^{W}\boldsymbol{p}_2 + \Delta\,{}^{W}\boldsymbol{p}_1 \end{aligned} \tag{12}$$

where symbols $\Delta\,{}^{W}\boldsymbol{p}_1$, $\Delta\,{}^{W}\boldsymbol{p}_2$ and $\Delta\,{}^{W}\boldsymbol{p}_3$ denote the position errors caused by hand-eye, robot and matching pose errors, respectively. For a general pose ${}^{N}_{M}\boldsymbol{T}$, the pose error matrix $\Delta\,{}^{N}_{M}\boldsymbol{T}$ can be written as

$$\Delta\,{}^{N}_{M}\boldsymbol{T} = {}^{N}_{M}\boldsymbol{T}\,{}^{M}\Delta \tag{13}$$

where symbol

$${}^{M}\Delta = [{}^{M}\boldsymbol{D}] = \begin{bmatrix} [{}^{M}\boldsymbol{\delta}] & {}^{M}\boldsymbol{d} \\ \boldsymbol{0}_{1\times3} & 0 \end{bmatrix} \tag{14}$$

is a 4×4 differential error matrix. In Fig. 2, symbol ${}^{M}\boldsymbol{d}$ is the 3×1 position error, symbol ${}^{M}\boldsymbol{\delta}$ is the 3×1 rotation error, and symbol

$${}^{M}\boldsymbol{D} = \begin{bmatrix} {}^{M}\boldsymbol{d} \\ {}^{M}\boldsymbol{\delta} \end{bmatrix} \tag{15}$$

is the pose error vector of the matrix $\Delta\,{}^{N}_{M}\boldsymbol{T}$. Vector ${}^{M}\boldsymbol{D}$ has the operators ${}^{M}\boldsymbol{D} = ({}^{M}\Delta)^{\vee}$ and ${}^{M}\Delta = [{}^{M}\boldsymbol{D}]$. Thus, three pose error matrices $\Delta\,{}^{E}_{S}\boldsymbol{T}$, $\Delta\,{}^{B}_{E}\boldsymbol{T}$ and $\Delta\,{}^{W}_{B}\boldsymbol{T}$ correspond to three pose error

vectors (${}^{S}\boldsymbol{D}$, ${}^{E}\boldsymbol{D}$ and ${}^{B}\boldsymbol{D}$), respectively. In the following, the linear relationship between the position errors ($\Delta^{W}\boldsymbol{p}_1$, $\Delta^{W}\boldsymbol{p}_2$ and $\Delta^{W}\boldsymbol{p}_3$) and (${}^{S}\boldsymbol{D}$, ${}^{E}\boldsymbol{D}$ and ${}^{B}\boldsymbol{D}$) is derived.

Part 1: hand-eye pose error

According to (12), there is

$$\Delta^{W}\boldsymbol{p}_1=({}^{W}_{S}\boldsymbol{T}[{}^{S}\boldsymbol{D}]{}^{W}_{S}\boldsymbol{T}^{-1}){}^{W}_{S}\boldsymbol{T}\,{}^{S}\boldsymbol{p} \tag{16}$$

According to $[\mathrm{Ad}_{\mathrm{V}}({}^{N}_{M}\boldsymbol{T})\,{}^{M}\boldsymbol{D}]={}^{N}_{M}\boldsymbol{T}[{}^{M}\boldsymbol{D}]{}^{N}_{M}\boldsymbol{T}^{-1}$, there is

$$\begin{aligned}\Delta^{W}\boldsymbol{p}_1&=({}^{W}_{S}\boldsymbol{T}[{}^{S}\boldsymbol{D}]{}^{W}_{S}\boldsymbol{T}^{-1}){}^{W}_{S}\boldsymbol{T}\,{}^{S}\boldsymbol{p}\\&=[\mathrm{Adv}({}^{W}_{S}\boldsymbol{T})\,{}^{S}\boldsymbol{D}]^{W}\boldsymbol{p}\end{aligned} \tag{17}$$

where

$$\mathrm{Ad}_{\mathrm{V}}({}^{W}_{S}\boldsymbol{T})\,{}^{S}\boldsymbol{D}=\begin{bmatrix}{}^{W}_{S}\boldsymbol{R}\,{}^{S}\boldsymbol{d}+[{}^{W}\boldsymbol{t}_{S}]{}^{W}_{S}\boldsymbol{R}\,{}^{S}\boldsymbol{\delta}\\ {}^{W}_{S}\boldsymbol{R}\,{}^{S}\boldsymbol{\delta}\end{bmatrix} \tag{18}$$

is the operator of the speed adjoint transformation. By substituting (18) into (17), there is

$$\begin{aligned}\Delta^{W}\boldsymbol{p}_1&=[{}^{W}_{S}\boldsymbol{R}\,{}^{S}\boldsymbol{\delta}]^{W}\boldsymbol{p}+{}^{W}_{S}\boldsymbol{R}\,{}^{S}\boldsymbol{d}+[{}^{W}\boldsymbol{t}_{S}]{}^{W}_{S}\boldsymbol{R}\,{}^{S}\boldsymbol{\delta}\\&=\begin{bmatrix}{}^{W}_{S}\boldsymbol{R},\ [{}^{W}\boldsymbol{t}_{S}-{}^{W}\boldsymbol{p}]{}^{W}_{S}\boldsymbol{R}\end{bmatrix}\begin{bmatrix}{}^{S}\boldsymbol{d}\\ {}^{S}\boldsymbol{\delta}\end{bmatrix}=\boldsymbol{M}_1\,{}^{S}\boldsymbol{D}\end{aligned} \tag{19}$$

Part 2: robot pose error

According to (12), the position error caused by robot pose error ${}^{E}\boldsymbol{D}$ is

$$\Delta^{W}\boldsymbol{p}_2={}^{W}_{B}\boldsymbol{T}\Delta{}^{B}_{E}\boldsymbol{T}\,{}^{E}_{S}\boldsymbol{T}\,{}^{S}\boldsymbol{p}=[\mathrm{Ad}_{\mathrm{V}}({}^{W}_{E}\boldsymbol{T})\,{}^{E}\boldsymbol{D}]^{W}\boldsymbol{p} \tag{20}$$

Similar to (17)-(19), equation (20) can be written as

$$\Delta^{W}\boldsymbol{p}_2=\begin{bmatrix}{}^{W}_{E}\boldsymbol{R},\ [{}^{W}\boldsymbol{t}_{E}-{}^{W}\boldsymbol{p}]{}^{W}_{E}\boldsymbol{R}\end{bmatrix}\begin{bmatrix}{}^{E}\boldsymbol{d}\\ {}^{E}\boldsymbol{\delta}\end{bmatrix}=\boldsymbol{M}_2\,{}^{E}\boldsymbol{D} \tag{21}$$

In addition, the robot pose error ${}^{E}\boldsymbol{D}$ is caused by kinematic errors $\Delta\boldsymbol{Q}$ in (2). By taking the partial derivatives with respect to each kinematic parameter q_i , the robot pose error vector can be written as

$$\begin{aligned}{}^{E}\boldsymbol{D}&=({}^{E}\Delta)^{\vee}=({}^{B}_{E}\boldsymbol{T}^{-1}\Delta{}^{B}_{E}\boldsymbol{T})^{\vee}=\sum_{i=1}^{4m}\left({}^{B}_{E}\boldsymbol{T}^{-1}\frac{\partial{}^{B}_{E}\boldsymbol{T}}{\partial q_i}\right)^{\vee}\Delta q_i\\&=\begin{bmatrix}\left({}^{B}_{E}\boldsymbol{T}^{-1}\frac{\partial{}^{B}_{E}\boldsymbol{T}}{\partial q_1}\right)^{\vee},\cdots,\left({}^{B}_{E}\boldsymbol{T}^{-1}\frac{\partial{}^{B}_{E}\boldsymbol{T}}{\partial q_{4m}}\right)^{\vee}\end{bmatrix}\begin{bmatrix}\Delta q_1\\ \vdots\\ \Delta q_{4m}\end{bmatrix}\\&=\boldsymbol{K}\Delta\boldsymbol{Q}\end{aligned} \tag{22}$$

By substituting (22) into (21), there is

$$\Delta^{W}\boldsymbol{p}_2=\boldsymbol{M}_2\,{}^{E}\boldsymbol{D}=\boldsymbol{M}_2\boldsymbol{K}\Delta\boldsymbol{Q} \tag{23}$$

Part 3: matching pose error

Similar to (19), the position error $\Delta^{W}\boldsymbol{p}_3$ caused by matching pose error can be written as

$$\Delta^{W}\boldsymbol{p}_3=\begin{bmatrix}{}^{W}_{B}\boldsymbol{R},\ [{}^{W}\boldsymbol{t}_{B}-{}^{W}\boldsymbol{p}]{}^{W}_{B}\boldsymbol{R}\end{bmatrix}{}^{B}\boldsymbol{D}=\boldsymbol{M}_3\,{}^{B}\boldsymbol{D} \tag{24}$$

Combining (19), (23) and (24), there is

$$\begin{aligned}\Delta^{W}\boldsymbol{p}&=\boldsymbol{M}_3\,{}^{B}\boldsymbol{D}+\boldsymbol{M}_2\,{}^{E}\boldsymbol{D}+\boldsymbol{M}_1\,{}^{S}\boldsymbol{D}\\&=[\boldsymbol{M}_3,\boldsymbol{M}_2\boldsymbol{K},\boldsymbol{M}_1][{}^{B}\boldsymbol{D}^{\mathrm{T}},\Delta\boldsymbol{Q}^{\mathrm{T}},{}^{S}\boldsymbol{D}^{\mathrm{T}}]^{\mathrm{T}}=\boldsymbol{M}\boldsymbol{\xi}\end{aligned} \tag{25}$$

where $\boldsymbol{M}$ is a $3\times(4m+12)$ coefficient matrix, and $\boldsymbol{\xi}$ is an error vector including hand-eye pose error ${}^{S}\boldsymbol{D}$, kinematic errors $\Delta\boldsymbol{Q}$ and matching pose error ${}^{B}\boldsymbol{D}$.

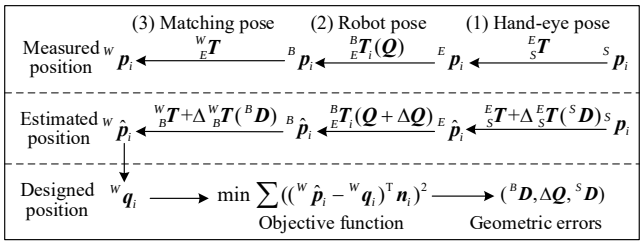

Fig. 3. Principle of geometry error identification. The designed point ${}^{W}\boldsymbol{q}_i$ is obtained by searching the closest point of point ${}^{W}\boldsymbol{p}_i$ on design model.

B. Geometry error identification

The principle of geometry error calibration is shown in Fig. 3. According to (25), the estimated value of the reconstructed point ${}^{W}\boldsymbol{p}_i$ considering geometry error is ${}^{W}\hat{\boldsymbol{p}}_i={}^{W}\boldsymbol{p}_i+\Delta^{W}\boldsymbol{p}_i$. The closest point of ${}^{W}\boldsymbol{p}_i$ in design model is defined as ${}^{W}\boldsymbol{q}_i$. In general, the residual e_i between the designed and estimated values is expressed as the point-to-point distance $\|{}^{W}\hat{\boldsymbol{p}}_i-{}^{W}\boldsymbol{q}_i\|_2$. However, there is only linear convergence speed in the iteration process [33]. For fast convergence speed, the point-to-tangent distance is used to express the residual

$$\begin{aligned}e_i&=({}^{W}\hat{\boldsymbol{p}}_i-{}^{W}\boldsymbol{q}_i)^{\mathrm{T}}\boldsymbol{n}_i\\&=\boldsymbol{n}_i^{\mathrm{T}}({}^{W}\boldsymbol{p}_i-{}^{W}\boldsymbol{q}_i)+\boldsymbol{n}_i^{\mathrm{T}}\boldsymbol{M}_i\boldsymbol{\xi}\end{aligned} \tag{26}$$

where $\boldsymbol{n}_i$ is the unit normal vector of ${}^{W}\boldsymbol{q}_i$. To identify the pose errors, the objective function is defined as

$$\min\ f({}^{B}\boldsymbol{D},\Delta\boldsymbol{Q},{}^{S}\boldsymbol{D})=\sum_{i=1}^{n\times m}e_i^2(\boldsymbol{\xi})=c+\boldsymbol{\xi}^{\mathrm{T}}\boldsymbol{A}\boldsymbol{\xi}+2\boldsymbol{b}\boldsymbol{\xi} \tag{27}$$

which denotes the sum of the squared residual e_i between the estimated position ${}^{W}\hat{\boldsymbol{p}}_i$ and the designed position ${}^{W}\boldsymbol{q}_i$ in frame $\{W\}$, as shown in Fig. 3. Estimated position ${}^{W}\hat{\boldsymbol{p}}_i$ is corrected on the basis of the initial measurement value ${}^{W}\boldsymbol{p}_i$ considering the geometry errors $\boldsymbol{\xi}$ to be determined. Designed position ${}^{W}\boldsymbol{q}_i$ is the closest point of ${}^{W}\boldsymbol{p}_i$ on design model. The residual e_i is expressed as point-to-tangent distance for second order convergence. There are $n\times m$ points participating in the construction of the objective function, which contributing to the calibration performance. By minimizing the function, the calculated geometry error is

$$\boldsymbol{\xi}=-\boldsymbol{A}^{-1}\boldsymbol{b}^{\mathrm{T}} \tag{28}$$

Then the hand-eye pose error, kinematic errors and matching pose error can be calculated by $\boldsymbol{\xi}$.

The function (27) is equivalent to $f=\sum e_i^2(\boldsymbol{\xi})$ where $\boldsymbol{e}(\boldsymbol{\xi})=[e_1(\boldsymbol{\xi}),\cdots e_{n\times m}(\boldsymbol{\xi})]^{\mathrm{T}}$. Using Gaussian-Newton method,

the iterative solution of minimizing f is

$$\boldsymbol{\xi}_{G-N}=-(\nabla \boldsymbol{e}^{\mathrm{T}}(\xi_0)\nabla \boldsymbol{e}(\xi_0))^{-1}\nabla \boldsymbol{e}^{\mathrm{T}}(\xi_0)\boldsymbol{e}(\xi_0) \tag{29}$$

where $\boldsymbol{\xi}_0=\mathbf{0}$ is the initial value of $\boldsymbol{\xi}$, $\nabla \boldsymbol{e}(\xi_0)$ is the gradient. It can be obtained that the solution using Gaussian Newton method is $\boldsymbol{\xi}_{G-N}==\boldsymbol{\xi}$. Thus, the iterative solution $\boldsymbol{\xi}$ in (28) is equivalent to the solution $\boldsymbol{\xi}_{G-N}$ based on Gaussian-Newton method that has a second-order convergence speed.

C. Geometry error compensation

Using the identified geometry errors, the compensated geometry parameters can be written as

$${}^{N}_{M}\hat{\boldsymbol{T}}={}^{N}_{M}\boldsymbol{T}+\Delta {}^{N}_{M}\boldsymbol{T}={}^{N}_{M}\boldsymbol{T}\,\mathrm{Tran}({}^{M}\boldsymbol{d})\,\mathrm{Rot}({}^{M}\boldsymbol{\delta}) \tag{30}$$

where $\mathrm{Tran}({}^{M}\boldsymbol{d})$ and $\mathrm{Rot}({}^{M}\boldsymbol{\delta})$ are the 4×4 differential translation and rotation matrices, respectively. The reconstructed measured point can be updated as

$${}^{W}\hat{\boldsymbol{p}}_i={}^{W}_{B}\hat{\boldsymbol{T}}\,{}^{B}_{E}\hat{\boldsymbol{T}}_i(\boldsymbol{Q}+\Delta\boldsymbol{Q})\,{}^{E}_{S}\hat{\boldsymbol{T}}\,{}^{S}\boldsymbol{p}_i \tag{31}$$

The closest distance from ${}^{W}\hat{\boldsymbol{p}}_i$ to design model is defined as e_i. The calibration accuracy can be defined as the average error and standard deviation error of e_i. The process can be calibrated iteratively for a higher calibration accuracy. The steps are as follows.

1) Data acquisition. Robot pose is changed randomly to collect point sets ${}^{S}P=\{{}^{S}P_1,\cdots,{}^{S}P_n\}$ and poses $\Gamma=\{{}^{B}_{E}\boldsymbol{T}_1,\cdots,{}^{B}_{E}\boldsymbol{T}_n\}$.
2) Initialization. The coarse calibrated results are substituted into (3) to reconstruct the set ${}^{W}P$.
3) Searching closest point. For each reconstructed measured point ${}^{W}\boldsymbol{p}_i$, closest point search algorithm (such as kdtree) is used to find the corresponding closest point ${}^{W}\boldsymbol{q}_i$ of ${}^{W}\boldsymbol{p}_i$ in design model.
4) Geometry error identification. Equations (19)- (28) are used to calculate the geometry error vector $\boldsymbol{\xi}$.
5) Geometry error compensation. Equation (30) is used to calculate the compensated geometry parameters. Equation (31) is used to calculate the updated point.
6) Iterative calibration. Initial poses (${}^{W}_{B}\boldsymbol{T}={}^{W}_{B}\hat{\boldsymbol{T}}$, ${}^{E}_{S}\boldsymbol{T}={}^{E}_{S}\hat{\boldsymbol{T}}$ and ${}^{B}_{E}\boldsymbol{T}={}^{B}_{E}\hat{\boldsymbol{T}}_i$) and point set ${}^{W}P={}^{W}\hat{P}$ are replaced . Repeat steps 3) – 5) until the number of iterations are larger than the given threshold.

According to above steps, it is concluded that :1) Step 1 shows the convenience of the calibration process, since it allows the measured points to be collected from random robot poses, without the need for specific pose control. 2) Each area of the free-form surface can be scanned to collect the measured points. Thus, the size of the free-form surface is not limited by the scope of the vison sensor, which is appropriate for the calibration in a large space. 3) When the measured error of the workpiece (aero blades, cranks) is large, the workpiece can be used as the calibration object to trace the error sources in (25). This is an advantage compared to the calibration methods using regular calibration objects. For n measured point sets with m points in each set, the comparison is concluded in Table I.

TABLE I
COMPARISON OF CALIBRATION METHODS

Method	Sphere-based method	Proposed method
Calibration object	Standard sphere	Free-form surface
World frame	Base frame $\{B\}$	Design model frame $\{W\}$
Feature point	Sphere center ${}^{B}\boldsymbol{p}$: random and unknown in $\{B\}$	Each point ${}^{W}\boldsymbol{p}_{ij}$ on surface: fixed and known in $\{W\}$
Point number	$1\times m$	$n\times m$
Objective function	$\sum_{i=1}^{n-1}\left\|{}^{B}\hat{\boldsymbol{p}}_i-{}^{B}\hat{\boldsymbol{p}}_{i+1}\right\|^2$	$\sum_{i=1}^{n\times m}({}^{W}\hat{\boldsymbol{p}}_i-{}^{W}\boldsymbol{q}_i)^{\mathrm{T}}\boldsymbol{n}_i)^2$
Residual	$\left\|{}^{B}\hat{\boldsymbol{p}}_i-{}^{B}\hat{\boldsymbol{p}}_{i+1}\right\|$	$({}^{W}\hat{\boldsymbol{p}}_i-{}^{W}\boldsymbol{q}_i)^{\mathrm{T}}\boldsymbol{n}_i$
Residual type	Point-to-point distance	Point-to-tangent distance
Iteration speed	Linear	Second-order

It should be noted that: 1) Because of the incorporation of shape matching algorithm, the proposed method requires that the calibration object does not have infinite matching solutions. Thus, sphere and cylinder would not work in the proposed method. Sphere-based method is also not a special case of the proposed method. 2) The surface complexity mainly affects the calibration accuracy by affecting the matching results. In general, the surface complexity has little effect on the matching accuracy. Thus, the calibration accuracy would not have large difference between simple and complex free-form surfaces. 3) The data for calibration is the measured points of the free-form surface, rather than 2D image captured by the camera. Thus, vision sensor in the proposed method mainly focuses on the 3D scanner.

V. SIMULATION

According to the calibration process, the data to be collected for calibration are a set of measured points ${}^{S}P_i$ and corresponding robot pose ${}^{B}_{E}\boldsymbol{T}_i$. The measuring noise of set (${}^{S}P_i$) and the repeated positioning error of pose (${}^{B}_{E}\boldsymbol{T}_i$) affects the calibration performance and are hard to avoid. Thus, the sensitivity of proposed calibration method on the measuring noise, repeated positioning error and the data scale (number n of pairs (${}^{B}_{E}\boldsymbol{T}_i$, ${}^{S}P_i$)) are tested with the sphere-based method as a comparison.

A. Initialization

The vision-based robot system is shown in Fig. 1(a). The designed hand-eye and matching poses are:

${}^{E}_{S}\boldsymbol{T}^{*}:{}^{E}\boldsymbol{t}^{*}_{S}=[20,30,150]^{\mathrm{T}}$ mm, ${}^{E}\boldsymbol{E}^{*}_{S}=[0,0,0]^{\mathrm{T}}$ rad

${}^{W}_{B}\boldsymbol{T}^{*}:{}^{W}\boldsymbol{t}^{*}_{B}=[0,120,500]^{\mathrm{T}}$ mm, ${}^{W}\boldsymbol{E}^{*}_{B}=[0.5\pi,0,0]^{\mathrm{T}}$ rad

where ${}^{E}\boldsymbol{E}_{S}$ and ${}^{W}\boldsymbol{E}_{B}$ are the rotation vectors. The nominal joint parameters $\boldsymbol{Q}$ of the ABB 6650S robot with 6 DoFs are given in [1].The coarse calibrated pose errors are

${}^{S}\boldsymbol{D}$: ${}^{S}\boldsymbol{d}=[-0.01,-0.01,-0.01]^{\mathrm{T}}$ mm,
${}^{S}\boldsymbol{\delta}=[-0.0175,-0.0175,-0.0175]^{\mathrm{T}}\times10^{-3}$ rad,

${}^{B}\boldsymbol{D}$: ${}^{B}\boldsymbol{d}=[-0.01,-0.01,0.01]^{\mathrm{T}}$ mm
${}^{B}\boldsymbol{\delta}=[-0.175,-0.175,0.175]^{\mathrm{T}}\times10^{-3}$ rad

This article has been accepted for publication in a future issue of this journal, but has not been fully edited. Content may change prior to final publication. Citation information: DOI 10.1109/TIE.2021.3090716, IEEE Transactions on Industrial Electronics

The kinematic errors are given as $\Delta a_{i-1}=\Delta d_i=0.04$ mm and $\Delta\alpha_{i-1}=\Delta\theta_i=0.04\times10^{-3}$ rad, corresponding to the average robot position error $\varepsilon({}^B\boldsymbol{t}_E)=$ 0.255 mm and orientation error $\varepsilon({}^B\boldsymbol{E}_E)=$ 0.19×10^{-3} rad, respectively. Based on the initial parameters, both spherical and free-form surfaces in Fig. 4 are used to further finely identify the geometry parameters. The sphere and free-form surface a diameter d=60 mm and dimensions 307 mm × 204 mm × 124 mm, respectively. Both objects are fixed in the same position on base frame $\{B\}$.

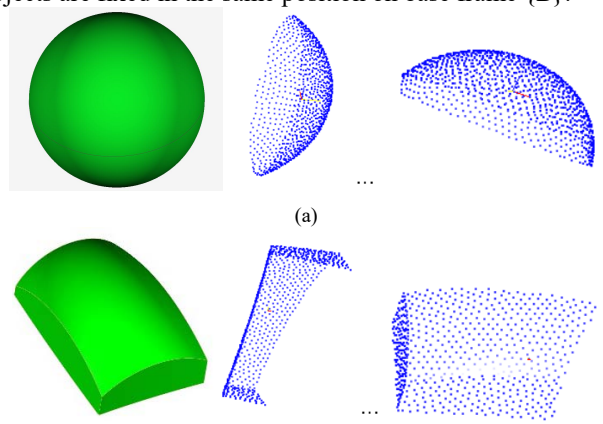

(a) (b)

Fig. 4. Two types of calibration objects. (a) Sphere. (b) Free-form surface. The design model ${}^W Q$ and the measured points $({}^S P_1,\cdots {}^S P_n)$ are shown in green and blue, respectively.

B. Measuring noise

It is assumed that the measuring noise has a Gaussian distribution $N(0,\ \sigma_m^2)$ [36]. Different measuring noise for standard deviation σ_m (0 mm–0.5 mm) is added in the normal direction of each measured point. The calibration error with respect to measuring noise is summarized in Fig. 5, showing that the free-form surface outperforms the standard sphere. The calibration error for sphere is positive to the measuring noise, particularly when σ_m >0.05 mm. For example, when σ_m =0.4 mm (Table II), the hand-eye calibration errors for sphere are large (0.061 mm versus 0.007 mm, 0.034×10^{-3} rad versus 0.005×10^{-3} rad), which even exceeds the error before fine calibration (0.02 mm, 0.03×10^{-3} rad). However, the calibration error for free-form surface is less sensitive to the measuring noise.

The reason is explained as follows. 1) Each measured point of the free-form surface can be used as the feature point. The free-form surface has many feature points (1000n versus n) in (27) for calibration, potentially reducing the effect of noise disturbance on the calibration result. 2) When the measuring noise is large, the calibration accuracy can also be reduced by multiple iterations until the calibration error is stationary. 3) The feature point (sphere center) of the sphere is obtained by spherically fitting each local point set ${}^S P_i$, rather than the global set ${}^S P$. The fitting accuracy is sensitive to the area of the set ${}^S P_i$. According to (27), the proposed method using the shape matching algorithm can be regarded as fitting the global measured points ${}^S P$ to the design model ${}^W Q$, which helps improve the fitting accuracy compared to local fitting.

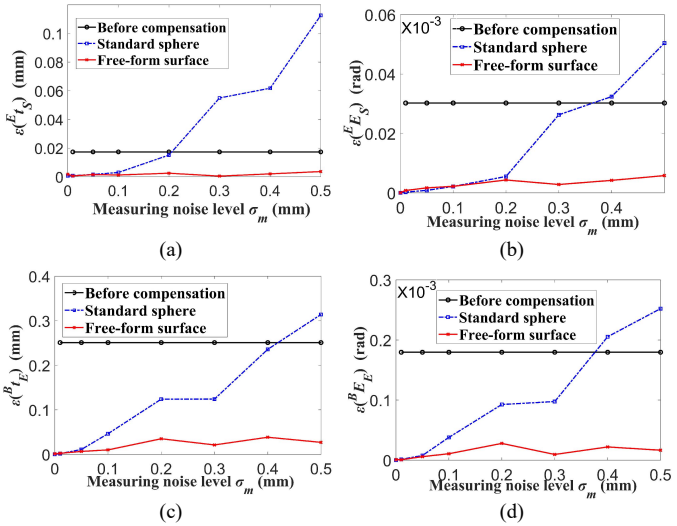

Fig. 5. Calibration errors of (a) hand-eye position $\varepsilon({}^E\boldsymbol{t}_S)$, (b) hand-eye orientation $\varepsilon({}^E\boldsymbol{E}_S)$, (c) robot position $\varepsilon({}^B\boldsymbol{t}_E)$, and (d) robot orientation $\varepsilon({}^B\boldsymbol{E}_E)$ with respect to measuring noise.

TABLE II
CALIBRATION ERROR COMPARISON FOR σ_M=0.4 MM

Calibration error	$\varepsilon({}^E\boldsymbol{t}_S)$ mm	$\varepsilon({}^E\boldsymbol{E}_S)$ 10^{-3} rad	$\varepsilon({}^B\boldsymbol{t}_E)$ mm	$\varepsilon({}^B\boldsymbol{E}_E)$ 10^{-3} rad
Sphere-based method	0.061	0.034	0.236	0.205
Proposed method	0.007	0.005	0.038	0.022

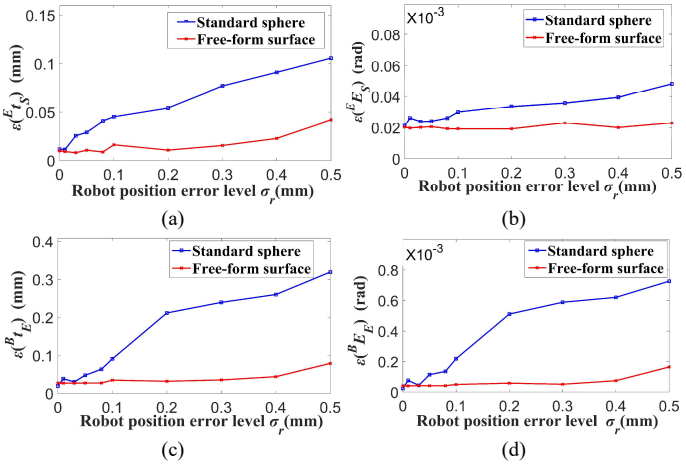

Fig. 6. Four calibration errors of (a) hand-eye position, (b) hand-eye orientation, (c) robot position and (d) robot orientation with respect to robot positioning error level σ_r.

C. Robot positioning error

Repeated positioning error is an important robot index and usually has a Gaussian distribution [37, 38]. Thus, noise $N(0,\sigma_r^2)$ with σ_r = 0 mm - 0.5 mm is added to three coordinate components of the robot position ${}^B\boldsymbol{t}_E$ to simulate the positioning error. The calibration error with respect to positioning error level σ_r is shown in Fig. 6. Except the calibrated hand-eye orientation, the other three calibrated parameters using sphere are sensitive to the robot positioning error. In the proposed method using free-form surface, four

This article has been accepted for publication in a future issue of this journal, but has not been fully edited. Content may change prior to final publication. Citation information: DOI 10.1109/TIE.2021.3090716, IEEE Transactions on Industrial Electronics

calibrated pose errors only have a minus increase when the deviation σ_r increases. The reason is explained as follows. 1) For each robot pose ${}^{B}_{E}\boldsymbol{T}_i$, the free-form surface has many feature points for calibration, making full use of the robot poses and reducing the effect of robot positioning error on calibration result. 2) Multiple iterations help reduce the calibration error under a large positioning error and a limited number of robot poses.

D. Data scale

The calibration errors with respect to the number n of pairs $({}^{B}_{E}\boldsymbol{T}_i, {}^{S}P_i)$ are tested. The result is shown in Fig. 7. The calibration error of the robot pose converges more slowly than that of the hand-eye pose because of more pose parameters (24 versus 6). When n is changed from 40 to 80, the calibration errors based on free-form surface quickly decrease to a stable value. However, the calibration errors of the sphere-based method requires more data (≥4000) for stable values. Thus, the proposed method needs less data $({}^{B}_{E}\boldsymbol{T}_i, {}^{S}P_i)$ and less work on robot operation to achieve the same calibration accuracy. Another reason is the large range distribution of featuring points. The sphere size (60 mm) is limited by the scope of the vision sensor to ensure sphere fitting accuracy. In contrast, the fitting accuracy and the size of free-form surface are not affected by the scope of the vision sensor due to global fitting. A large size (307 mm × 204 mm × 274 mm) ensures a large range distribution of feature points and a large movement range of the robot, potentially reducing calibration errors. This conclusion also revealed that free-form surface is appropriate for large space calibration to measure large objects, such as ship propellers, nuclear blades and aircraft wings.

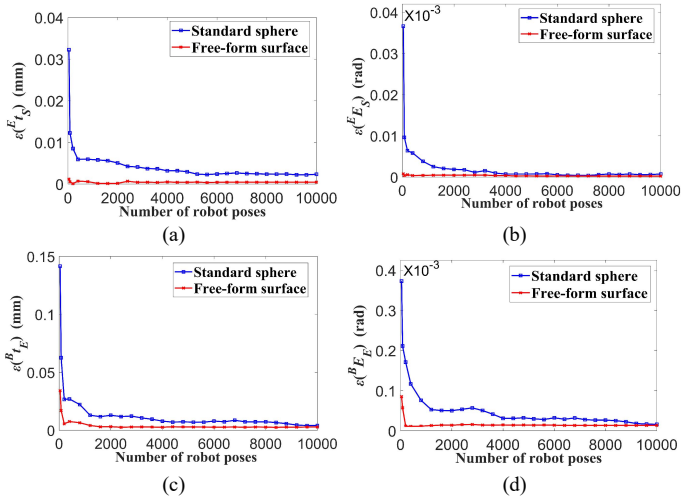

Fig. 7. Calibration error of (a) hand-eye position $\varepsilon({}^{E}\boldsymbol{t}_S)$, (b) hand-eye orientation $\varepsilon({}^{E}\boldsymbol{E}_S)$, (c) robot position $\varepsilon({}^{B}\boldsymbol{t}_E)$ and (d) robot orientation $\varepsilon({}^{B}\boldsymbol{E}_E)$ with respect to number n of pairs $({}^{B}_{E}\boldsymbol{T}_i, {}^{S}P_i)$.

VI. Experiment

In Fig. 8, the vision-based robot system consists of an ABB 1600 robot and a Power-Scan surface scanner with measurement accuracy of ±0.015 mm. The hand-eye pose ${}^{E}_{S}\boldsymbol{T}$ is first calibrated using the sphere. To further improve the calibration accuracy, two different blades are used as calibration objects. The blades are fixed at the ground and are scanned randomly in 120 robot poses to obtain the measured point sets [Fig. 9(a)] that are reconstructed using the initial hand-eye pose ${}^{E}_{S}\boldsymbol{T}$. Reconstructed points ${}^{W}P$ are matched to the design model to obtain the initial matching pose ${}^{W}_{B}\boldsymbol{T}$ and the closest point set ${}^{W}Q$. Using the measured points ${}^{W}P$, closest points ${}^{W}Q$ and initial poses $({}^{W}_{B}\boldsymbol{T}, {}^{B}_{E}\Gamma(\boldsymbol{Q}), {}^{E}_{S}\boldsymbol{T})$, the geometry errors are identified using (28). The geometry parameters are compensated using (30), and the measured points are compensated using (31). By comparing the compensated measured points ${}^{W}P'$ with the design model ${}^{W}Q$, the average (Ave) and standard deviation (Std) errors are calculated for accuracy evaluation.

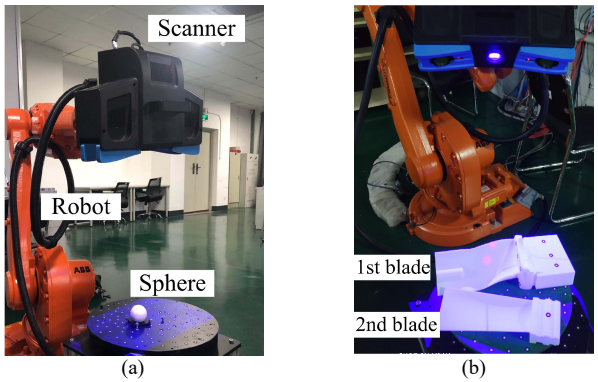

Fig. 8. Vision-based robot system using different calibration objects. (a) Using sphere as calibration object. (b)Using two blades as calibration objects.

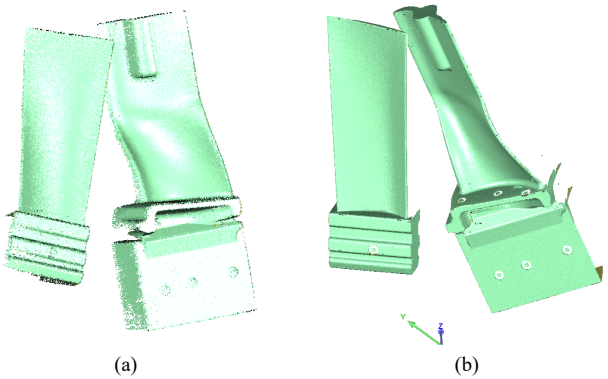

Fig. 9. Reconstructed measured points using (a) sphere and (b) the first blade as calibration object.

Fig. 10 shows the std error of the first blade with respect to iterations of geometry error identification. The position error in (27) are expressed as both point-to-point and point-to-tangent distances to calculate the geometry errors. The point-to-tangent distance converges much faster than the point-to-point distance. It takes only 2 iterations. This result verifies that 1) the solution using the point-to-tangent distance shows second-order convergence. When sphere is used as calibration object, more

This article has been accepted for publication in a future issue of this journal, but has not been fully edited. Content may change prior to final publication. Citation information: DOI 10.1109/TIE.2021.3090716, IEEE Transactions on Industrial Electronics

iterations are needed because of the point-to-point distance between sphere centers. 2) Multiple iterations help improve the calibration accuracy. After 7 iterations, the final identified geometry error using the point-to-tangent distance is shown in Table III. The compensated points are shown in Fig. 9(b). Compared with the sphere-based result in Fig. 9(a), the surface quality is obviously improved. The reconstructed measured points for two methods are compared with the design model to generate the error map. The results are shown in Fig. 11-12 and Table IV. The std and average errors based on the two blades object are smaller than that of sphere-based method. The similar calibration results of the two blades show that general free-form surfaces can be used as calibration object.

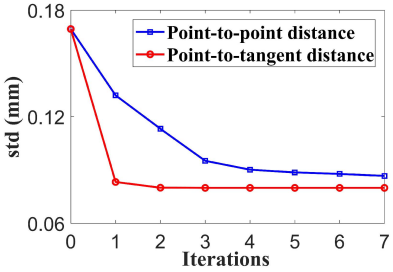

Fig. 10. Std error with respect to the iterations for the first blade as calibration object. The residuals based on point-to-point and point-to-tangent distances are compared.

TABLE III
IDENTIFIED GEOMETRY ERROR BY USING FIRST BLADE AS CALIBRATION OBJECT

j-th joint	1	2	3	4	5	6
Δa_{j-1} (mm)	0	0.008	0.015	–0.003	–0.015	–0.008
$\Delta\alpha_{j-1}$ (10^{-3} rad)	0.001	–0.007	–0.012	0.012	0.005	0.010
Δd_j (mm)	0	–0.013	0	0.012	–0.009	0
$\Delta\theta_j$ (10^{-3} rad)	–0.016	0.012	0.016	0.009	–0.022	0
${}^{S}\boldsymbol{D}$	${}^{S}\boldsymbol{d}$ =[0.107, 0.062, 0.024], ${}^{S}\boldsymbol{\delta}$=[0.106,0.002, –0.030]×$10^{-3}$					
${}^{B}\boldsymbol{D}$	${}^{B}\boldsymbol{d}$ =[–0.351, 0.064, 0.121], ${}^{B}\boldsymbol{\delta}$=[0.063,0.118,0.087]×$10^{-3}$					

VII. CONCLUSION

This paper proposed a two-step geometry calibration method where the free-form surface is used as calibration object for both coarse and fine calibration. The convenient calibration procedure is presented to guide the operators. The calibration object allows free-form surfaces (blade, crank and complex mould) and regular objects that do not have infinite matching solutions. The fine calibration process acquires the measured points in a set of random robot poses, without the need for strict orientation/position control and significantly facilitating the operations. The accuracy and robustness of the proposed method have been demonstrated by the experiments. The proposed method can also be extended to the hand-eye, kinematics and tool calibration of other motion system with multiple axes. This paper focuses on the calibration in static pose. In future works, it is expected to be used for dynamic calibration based on free-form surface. The information fusion technology would be introduced for robustness pose estimation to obtain the measured points.

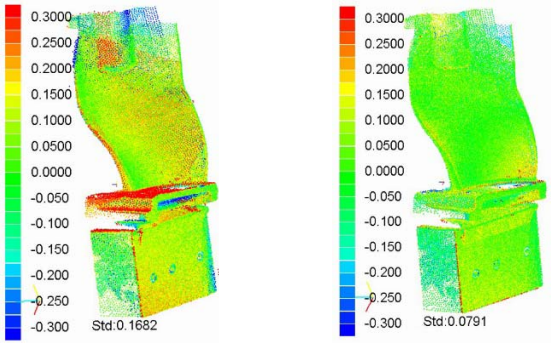

(a) (b)

Fig. 11. Error map of the first blade. (a) Sphere-based method; (b) Proposed method.

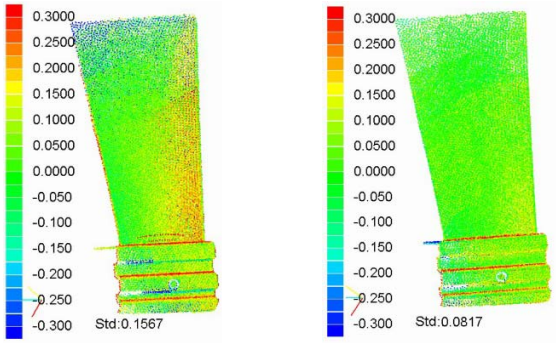

(a) (b)

Fig. 12. Error map of the second blade. (a) Sphere-based method; (b) Proposed method.

TABLE IV
MEASURING ERROR COMPARISON OF DIFFERENT METHODS (MM)

Blades	Measuring 1st blade		Measuring 2nd blade	
Error	Std	Ave	Std	Ave
Sphere-based method	0.155	0.165	0.143	0.157
Proposed method	0.102	0.079	0.098	0.082

REFERENCES

[1] W. Li, H. Xie, G. Zhang, S. Yan, and Z. Yin, "Hand-eye calibration in visually-guided robot grinding," *IEEE Trans. Cybern.*, vol. 46, no. 11, pp. 2634-2642, 2016.
[2] X. Xu, D. Zhu, H. Zhang, S. Yan, and H. Ding, "TCP-based calibration in robot-assisted belt grinding of aero-engine blades using scanner measurements," *Int. J. Adv. Manuf. Technol.*, vol. 90, no. 1, pp. 635-647, 2017.
[3] C. Moller, H. C. Schmidt, N. H. Shah, and J. Wollnack, "Enhanced absolute accuracy of an industrial milling robot using stereo camera system," presented at the *Int. Conf. on Sys.Integ. Intell.*, 2016.
[4] B. Mei, W. D. Zhu, K. Z. Yuan, and Y. L. Ke, "Robot base frame calibration with a 2D vision system for mobile robotic drilling," *Int. J. Adv. Manuf. Technol,* vol. 80, no. 9, pp. 1903-1917, 2015.
[5] Y. Zou and X. Chen, "Hand-eye calibration of arc welding robot and laser vision sensor through semidefinite programming," *Ind. Robot.*, vol. 45, no. 5, pp. 597-610, 2018.
[6] S. M. Luo, F. S. A. Li, P. J. Wang, Y. Yang, and J. Y. Mo, "Calibration method of roof weld coating robot system based on plane-to-plane intersection model," *Int. J. Precis. Eng. Manuf.*, pp. 1-11, 2020.
[7] W. Chang and C. Wu, "Eye-in-hand vision-based robotic bin-picking with active laser projection," *Int. J. Precis. Eng. Manuf.*, vol. 85, no. 9-12, pp. 2873-2885, 2016.
[8] L. C. Niu, L. Aha, J. Mattila, and E. Ruiz, "A stereoscopic eye-in-hand vision system for remote handling in ITER," *Fusion Eng. Des.*, vol. 146, pp. 1790-1795, 2019.
[9] S. Yin, Y. Ren, Y. Guo, J. Zhu, S. Yang, and S. Ye, "Development and calibration of an integrated 3D scanning system for high-accuracy large-scale metrology," *Measurement,* vol. 54, pp. 65-76, 2014.
[10] Y. J. Ren, S. B. Yin, and J. G. Zhu, "Calibration technology in application of robot-laser scanning system," *Opt. Eng.*, vol. 51, no. 11, pp. 42041-42046, 2012.
[11] C. Cajal, "A crenellated-target-based calibration method for laser triangulation sensors integration in articulated measurement arms," *Robot. Comput. Integr. Manuf.*, vol. 27, no. 2, pp. 282-291, 2011.
[12] K. Pachtrachai, F. Vasconcelos, F. Chadebecq, and M. Allan, "Adjoint transformation algorithm for hand-eye calibration with applications in robotic assisted surgery," *Ann.*

Biomed. Eng., vol. 46, no. 10, pp. 1606-1620, 2018.
[13] H. Su, C. G. Yang, H. Mdeihly, A. Rizzo, G. Ferrigno, and E. De Momi, "Neural network enhanced robot tool identification and calibration for bilateral teleoperation," *IEEE Access,* vol. 7, pp. 122041-122051, 2019.
[14] A. Malti and J. P. Barreto, "Robust hand-eye calibration for computer aided medical endoscopy," in *IEEE Int. Conf. on Rob. Autom.*, 2010, pp. 1-7.
[15] A. Nubiola and I. A. Bonev, "Absolute calibration of an ABB IRB 1600 robot using a laser tracker," *Robot. Comput. Integr. Manuf.,* vol. 29, no. 1, pp. 236-245, 2013.
[16] C. Li, Y. Wu, H. Löwe, and Z. Li, "POE-based robot kinematic calibration using axis configuration space and the adjoint error model," *IEEE Trans. Rob.,* vol. 32, no. 5, pp. 1264-1279, 2016.
[17] A. Tabb and K. M. Yousef, "Solving the robot-world hand-eye(s) calibration problem with iterative methods," *Mach. Vis. Appl.,* vol. 28, no. 5, pp. 569-590, 2017.
[18] M. Shah, "Solving the robot-world/hand-eye calibration problem using the Kronecker product," *J. Mech. Robot.* ., vol. 5, no. 3, pp. 1-7, 2013.
[19] L. Wu and H. Ren, "Finding the kinematic base frame of a robot by hand-eye calibration using 3D position data," *IEEE Trans. Autom. Sci. Eng.,* vol. 14, no. 1, pp. 314-324, 2017.
[20] G. Du, P. Zhang, D. Li. "Human–Manipulator Interface Based on Multisensory Process via Kalman Filters." *IEEE Trans. Ind. Electron.*, vol. 61, no. 10, pp. 5411 – 5418, 2014.
[21] G. Du, P. Zhang. A markerless human–robot interface using particle filter and Kalman filter for dual robots. *IEEE Ind. Electron.*,vol. 62, no. 4, pp.2257-2264,2015.
[22] J. Li *et al*., "Calibration of a multiple axes 3-D laser scanning system consisting of robot, portable laser scanner and turntable," *Optik,* vol. 122, no. 4, pp. 324-329, 2011.
[23] H. Xie, C. Pang, W. Li, Y. Li, and Z. Yin, "Hand-eye calibration and its accuracy analysis in robotic grinding," in *IEEE Int. Conf. Autom. Sci. Eng.*, 2015, pp. 862-867.
[24] Z. X. Xie, P. F. Zong, P. Yao, and P. Ren, "Calibration of 6-DOF industrial robots based on line structured light," *Optik,* vol. 183, pp. 1166-1178, 2019.
[25] A. Robertsson, "Six DOF eye-to-hand calibration from 2D measurements using planar constraints," in *IEEE/RSJ Int. Conf. Intell. Rob. Sys.*, 2015, pp. 1-5.
[26] Y. Y. Cai, H. Gu, C. Li, and H. Liu, "Easy industrial robot cell coordinates calibration with touch panel," *Robot. Comput.-Integr. Manuf.,* vol. 50, pp. 276-285, 2018.
[27] S. Sharifzadeh, I. Biro, and P. Kinnell, "Robust hand-eye calibration of 2D laser sensors using a single-plane calibration artefact," *Robot. Comput.-Integr. Manuf.,* vol. 61, pp. 1-10, 2020.
[28] W. Chen *et al*., "A noise-tolerant algorithm for robot-sensor calibration using a planar disk of arbitrary 3-D orientation," *IEEE Trans. Autom. Sci. Eng.,* vol. 15, no. 1, pp. 251-263, 2018.
[29] S. Reitelshofer and J. Franke, "Self-calibration method for a robot based 3D scanning System," in *Emerging Technologies and Factory Automation*, 2015, pp. 1-6.
[30] T. S. Lembono, F. Suarez-Ruiz, and Q. C. Pham, "SCALAR: simultaneous calibration of 2-D Laser and robot kinematic parameters using planarity and distance constraints," *IEEE Trans. Autom. Sci. Eng.,* vol. 16, no. 4, pp. 1971-1979, 2019.
[31] Y. Shibin, R. Yongjie, and Y. Shenghua, "A vision-based self-calibration method for robotic visual inspection systems," *Sensors,* vol. 13, no. 12, pp. 16565-16582, 2013.
[32] J.-S. Hu and Y.-J. Chang, "Automatic calibration of hand–eye–workspace and camera using hand-mounted line laser," *IEEE/ASME Trans. Mech.,* vol. 18, no. 6, pp. 1778-1786, 2013.
[33] H. Xie, W. Li, Z. Yin, and H. Ding, "Variance minimization iterative matching method for free-form surfaces—part I: theory and method," *IEEE Trans. Autom. Sci. Eng.,* vol. 16, no. 3, pp. 1181-1191, 2019.
[34] D. Holz, A. E. Ichim, F. Tombari, R. B. Rusu, and S. Behnke, "Registration with the point cloud library: a modular framework for aligning in 3-D," *IEEE Robot. Autom. Mag.,* vol. 22, no. 4, pp. 110-124, 2015.
[35] H. Pottmann, Q. X. Huang, Y. L. Yang, and S. M. Hu, "Geometry and convergence analysis of algorithms for registration of 3D shapes," *Int. J. Comput. Vis.,* vol. 67, no. 3, pp. 277-296, 2006.
[36] X. Huang, J. Zhang, L. Fan, Q. Wu, and C. Yuan, "A systematic approach for cross-source point cloud registration by preserving macro and micro structures," *IEEE Trans. Image Processing,* vol. 26, no. 7, pp. 3261-3276, 2016.
[37] X. Y. Chen, Q. J. Zhang, and Y. L. Sun, "Non-kinematic calibration of industrial robots using a rigid-flexible coupling error model and a full pose measurement method," *Robot. Comput. Integr. Manuf.,* vol. 57, pp. 46-58, 2019.
[38] I. Ali, O. Suominen, and E. R. Morales, "Methods for simultaneous robot world hand-eye calibration: a comparative study," *Sensors,* vol. 19, no. 12, pp. 1-16, 2019.

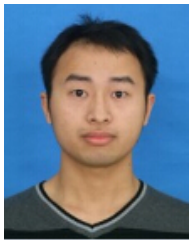

He Xie received a B.S. in mechanical design, manufacturing and automation from Huazhong University of Science & Technology (HUST), Wuhan, China, in 2013, and a Ph.D in mechatronic engineering from HUST in 2019. He is now a Postdoctoral in Hunan University, Changsha, China. His research interests include robotics and manufacturing automation.

Wenlong Li received a B.S. in mechanical engineering and automation from Xi'an Jiaotong University, Xi'an, China, in 2004, and a Ph.D. in mechatronic engineering from HUST, Wuhan, China, in 2010. He conducted the postdoctoral research in control engineering also at HUST in 2012. He is now a professor at HUST. His research interests include geometry inspection and robotic machining.

Hui Liu received the B.S. and Ph.D. degrees from the Central South University in 2004 and 2011, respectively. He received another Ph.D. degree from the University of Rostock, Germany in 2013. Now he is a professor in the Central South University and the University of Rostock. His research interests include robotics and artificial intelligence.